Vrije Universiteit Brussel

Document Version:
Submitted manuscript

Link to publication

Monte Carlo-based a-posteriori uncertainty quantification for Background-Oriented Schlieren measurements

Abdelhafidh MOUMEN · **Delphine LABOUREUR** · **Johan GALLANT** · **Patrick HENDRICK**

Abstract Background-Oriented Schlieren (BOS) is an optical visualization technique which reconstructs a whole-field flow based on its density gradient. BOS is similar to particle image velocimetry (PIV) in terms of experiments design and the computation of the displacements. However, in BOS, the reconstruction of the refraction index field involves further mathematical calculations, which depends on the flow geometry, such as Poisson solver, Abel inversion, algebraic reconstruction technique, and filtered back projection. This lengthy combination of experimental measurements, cross-correlation evaluation, and mathematical computation complicates the uncertainty quantification of the reconstructed field. In this study, we present a detailed approach for an a-posteriori estimation of uncertainty when using BOS to reconstruct the refractive index/density field. The proposed framework is based on Monte Carlo Simulation (MCS) method and can consider all kinds of sources of error, ranging from experimental measurements to image processing. The key features of this methodology are its capacity to handle different mathematical reconstruction procedures and the ease with which it can integrate additional sources of error. We demonstrate this method first by using synthetic images and a Poisson solver with mixed boundary conditions in a 2D domain. The accuracy of the proposed approach is assessed by comparing analytical and MCS results. Then, the modular nature of the proposed framework is experimentally demonstrated using a combination of Abel inversion and inverse gradient techniques to reconstruct a 3D axisymmetric density field around a supersonic projectile in free-flight. The results are compared with computational fluid dynamics (CFD) and show high levels of agreement with only limited discrepancies; this is probably due to the space-filtering effect within cross-correlation resulting from shocks waves.

Keywords Background-Oriented Schlieren · refraction index · density · uncertainty quantification · Monte Carlo · Poisson · Abel inversion

Abdelhafidh MOUMEN

Department of Weapon systems and Ballistics, Royal Military Academy, avenue de la Renaissance 30, Brussels, 1000, Belgium

Laboratory of Aero-Thermo-Mechanics, Université Libre de Bruxelles, avenue F.D. Roosevelt 50 (CP 165/41), Brussels, 1050, Belgium

E-mail: abdelhafidh.moumen@gmail.com

List of symbols

A, B	Uncertainty evaluation type
c_{50}	Covariance factor (overlap = 50%)
e_{ruler}	Ruler fabrication error
$e_{\Delta y}$	Total error in Δy computation
F	Refractive index reconstruction function
f	Lens focal length
G	Gladstone–Dale constant
h	Ambient humidity
k	Coverage factor
L	Length read on the ruler image
M	Background image magnification
Ma	Mach number
M_{obj}	Object plan image magnification
N_{eff}	effective number of pixels
N_s	Number of samples
N_T	Total number of a matrix elements
n	Refractive index
n_0	Reference refractive index
n_n	Normalized refractive index difference.
p	Ambient pressure
pix	Number of pixels that corresponds to L
r	Radial coordinate
s	Grid size in pixel
S	Poisson equation source term
σ	Distribution standard deviation
T	Ambient temperature
u	Standard uncertainty
u_c	Combined uncertainty
$U_\%$	Extended uncertainty
$\chi_\perp$	Component $\in (x, y)$ normal to the boundary
v	True assigned displacement in y-direction
Z_B	Distance object—background
Z_T	Distance camera—background
Z_W	Object width
$\mathcal{V}$	Extended vector
$\Delta x, y$	Displacements in the image plan
$\Delta x', y'$	Displacements in the background plan
δ	Elemental error
λ	Wavelength of light
$\varepsilon_{x,y}$	Light deflection in x,y direction
Ω	Real but unknown quantity value
ω	Elemental measurement
ρ	Density
τ	Background element particle image size

1 Introduction

Background Oriented Schlieren (BOS) is a density-based optical measurement technique. The recent development of this technique by Meier (1998) is a considerable progress in the capacity for quantitative flow visualization. BOS is increasingly employed in a broad range of areas ranging from ballistics (Moumen et al. (2020)) to aeronautics research (Raffel (2015)) thanks to its simplicity and low cost. Moreover, its large field of view has enabled to expand from laboratory to real-scale experiments (Hargather and Settles (2010)). Additionally, it is seen as a promising approach which can be employed as a validation tool for numerical code due to its non-intrusive nature and whole field measurement.

BOS is a similar and complementary investigation tool to PIV. However, it has a number of differentiating features. In BOS experiments, the particle displacement is due to an artificial distortion of image due to the local density gradient in between the camera and a fully controlled patterned background. As such, BOS is not affected by some of error sources found in PIV such as low seeding density or loss-of-pair (Raffel et al. (2018)). In contrast the reconstruction of the refraction index field through BOS requires additional computational procedures similar to the reconstruction of the velocity-based pressure field in PIV. These computation procedures can be categorized into three types (Raffel (2015)): First, Poisson equations for the $2D$ flows or $3D$ flows with prior knowledge of the flow dimensions (path integrated density). Second, Abel inversion for $3D$ axisymmetric flows. Finally, filtered back projection (FBP) or algebraic reconstruction technique (ART) or a mix of both for general 3D flows .

The measurement of refraction index (and subsequently the density) through BOS can be split into three successive steps:

– Measurements in the laboratory which includes the measurement of the setup dimensions and image acquisition
– The computation of the shift of background features determination using cross-correlation or optical flow algorithms.
– The reconstruction of the refraction index using one or a combination of the above-mentioned mathematical procedures

Consequently, the sources of error in the BOS technique can be divided into three groups, that correspond to its three-phases implementation. Firstly, the initial phase may cause several errors which are related to both the experimental setup as well as the medium. The errors in the experimental setup cover those due to the alignment and vibration, non-stability of the light source, and the optical layout dimensions measurement. Furthermore, the fluid may engender many errors due to the blurring effect, being out of focus, and the presence of important gradients such as the case of shock waves and boundary layers. Secondly, similarly to PIV, the evaluation algorithm causes errors on the computed displacement fields in both directions Δx and Δy, such as the presence of outliers, Space-filtering, and peak-locking effect. Thirdly, errors concerning mathematical procedures consisting of two parts: physical and numerical. The first part deals with the propagation of the inputs errors and how it contaminates the reconstructed refraction index field. The numerical errors as well cannot be ignored as they are twice present: on the approximations concerning the uncertainty propagation equations (i.e. truncation errors in Taylor Series expansion Method (TSM)) and on the computation schemes (e.g. finite difference schemes for Poisson solver).

As an experimental technique, BOS results are judged incomplete or even invalid whenever they are not supported by an uncertainty quantification. This quantification is an ex-

pression of the results' quality and a key component in all project stages ranging from the planning to the final results' evaluation. Moreover, the uncertainty quantification is relevant especially when the experimental results are used for numerical code validation. The latter can be rejected by an erroneous conclusion drawn from a validation comparison between experimental and numeric results.

Despite its relative simplicity, the fairly long BOS measurement chain, and subsequently the numerous error sources, makes the uncertainty quantification of the reconstructed refractive index field a laborious exercise. In addition, the uncertainty quantification may be biased by the possible existence of hidden errors and, more importantly, by the complexity of identifying and evaluating correlations between the identified errors. For example, to overcome the tedious task of identifying possible correlations in a steady-state case, the most reliable approach is to evaluate the final equation several times with multiple measurements and conclude on the uncertainty as a function of its distribution (Coleman and Steele (2009)). This is, of course, impractical in our case given the variety of fluids and processes involved, however, it is definitely conceivable by applying Monte Carlo Simulation (MCS) principle (JCGM (2008)).

We, therefore, intend to develop a MCS-based methodology for posterior uncertainty quantification on the refractive index/density field reconstructed using BOS. The final framework should handle the experimental, the cross-correlation, and the mathematical schemes uncertainties. Also, due to the diversity of the reconstruction mathematical approaches and the experimental performance techniques (e.g. use of a laser instead of white light and its inherent errors), the framework should be easily extensible and modular.

To the authors' best knowledge, there is only a single attempt in this area by Rajendran et al. (2019). The purpose of this unique effort was to quantify the uncertainty in the density field determined by BOS. The described methodology produces uncertainty bounds in the reconstructed field that are based on the displacement uncertainty propagation through the Poisson solver. Although this study is of particular importance as a pioneering work, it has several limitations. Indeed, it has only included the calculation using the Poisson solver without considering the other reconstructions methods. Moreover, the possible correlations between the different parameters were not taken into consideration.

To address a similar problem, which is PIV based quantities, various methods have been proposed on the PIV community. This is abundantly the case for the PIV-based pressure field computed using the Poisson equation. For instance, Pan et al. (2016) have examined the problem based on the Cauchy-Schwarz and Poincare inequalities. Through this study, the authors have shown that the error level on the pressure field can be bounded. Azijli et al. (2016) have considered the same problem by proposing an uncertainty quantification based on the Bayesian rule, which relies on prior knowledge of the velocity field proprieties based on its divergence error. Sciacchitano and Wieneke (2016) have presented uncertainty propagation formulas from PIV velocity measurements. Based on TSM, they have derived uncertainty equations for vorticity, divergence, Reynolds stress, and statistical quantities. Also, during their work, they have pointed out the significance of the spatial correlation between the errors on the displacements in the two directions.

From the above discussion, it can be inferred that, despite the complexity and the length of the BOS measurement chain, the uncertainty quantification by an analytical expression is conceivable. However, this conception is doubly disadvantageous. The main barrier to such implementation is the variety of the mathematical reconstruction procedure imposed by the flow nature. Indeed, the problem formulation in terms of the Poisson equation is certainly insufficient, conversely, this is a particular situation that requires a perfect knowledge of the
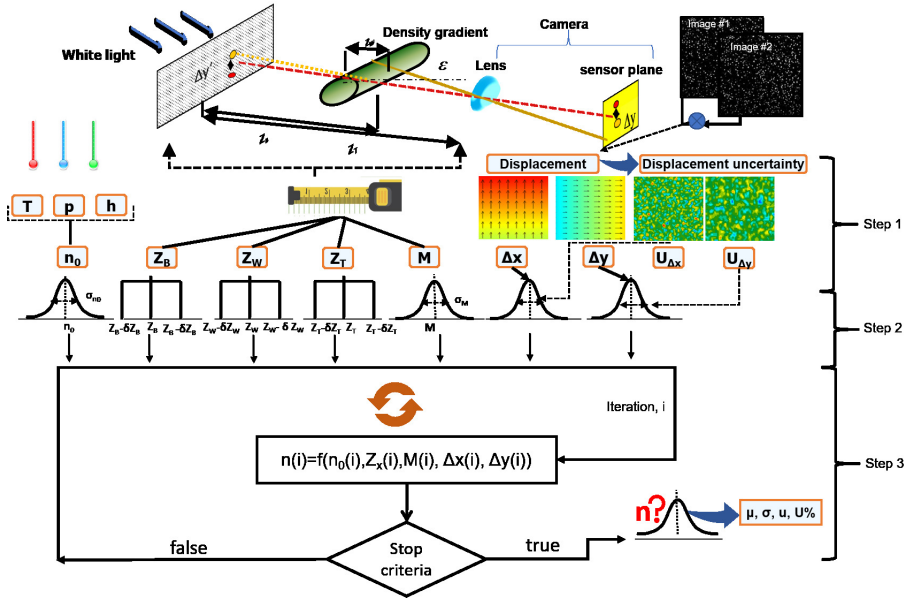
Fig. 1: Monte Carlo uncertainty quantification methodology for BOS.

flow dimensions, as well as adopting the assumption of a 2D flow where the ray deflection occurs at the median plane. For such an approach to be effective, it should be readily expandable into other mathematical procedures. The problem is more acute as the latter noticeably is increasing in number according to specific configurations, such as the use of ART combined with FBP (Hartmann and Seume (2016)) or the use of inverse gradient instead of the Poisson equation when derivation is not possible (presence of an object in the field). Another concern is that this kind of formulas requires the determination of correlation coefficients between errors.

Motivated by the need to create a flexible and customizable BOS uncertainty toolbox, in this work, we propose and implement an approach for uncertainty quantification of the refractive index/density fields in BOS based on the MCS. This method was chosen given that the integration of a new error source, studying its impact on the results or switching between the different mathematical processes of reconstruction are straightforward tasks. In addition, this method does not use the approximation and assumption that should be made when using the TSM, therefore, the JCGM (2008) considers it a more accurate technique and encourages using it at least once as a verification. This study represents a detailed investigation covering both errors on the displacement fields and those arising from the experimental measurements. The paper is composed of 6 sections: Sec. 2 presents the proposed methodology, Sec. 3 and 4 focus on the elementary uncertainties determination methods, Sec. 5 and 6 demonstrate and asses the methodology accuracy via a Poisson solver and Abel inversion algorithm on synthetic and experimental images, respectively.

2 Methodology

In BOS, the refraction index field n is not measured directly, instead it is calculated as a function F of several elemental measurements ω_i:

$$n = F(\omega_1, \omega_2, \omega_3 \ldots \omega_m) \tag{1}$$

Each of these measurements ω_i approximates the actual and unknown value Ω of the measured quantity. Therefore, it includes one or several error(s) δ_i that is/are associated with a specific elementary source of error. Hence, the uncertainty u, which is defined as the range of $\pm u$ around ω_i within which we think that Ω lies, is an indication of the measurement quality. The JCGM (2008) essentially distinguish three kinds of uncertainty. To describe this, let's assume that we are measuring a steady-state physical quantity. For N successive measurements, carried out under the same conditions and using the same instruments, we obtain N different results. This statistical evaluation outcomes follow a certain distribution (uniform, triangular, Gaussian...). This approach of error evaluation is referred to as Type A evaluation, whereas all other evaluations based on non-statistical procedures are referred to as Type B evaluation (JCGM (2008)). In the former, the further N tends towards infinity the closer the error distribution approaches that of the parent population, hence its mean and standard deviation (std). The standard uncertainty u is defined as the std of this measurement outcomes distribution, which is an estimate of the parent distribution std. To increase the confidence level that the true value lies inside the $\pm u$ interval, we can enlarge it by multiplying its bounds by a coverage factor k, thus obtaining the expanded uncertainty $U_\% = k_\% u$ where the subscript % is the given percent level of confidence. For instance, for a Gaussian distribution this factor is 1.0, 1.96, and 3.0 for a respective confidence degree of approximately 68.3%, 95%, and 99.7%. It should be noted that the Gaussian distribution is the most experienced in combined uncertainty, which is guaranteed by the standard central limit theorem (Coleman and Steele (2009)). Finally, the uncertainty in the refractive index is the propagation of the elemental standard uncertainties u_i via the function F, known as the combined uncertainty u_c.

To perform an uncertainty propagation evaluation, the JCGM (2008) recommends the TSM. The TSM is based on the first-order Taylor series expansion of the refraction index function F (Eq. 1) and can be expressed as:

$$u_c^2 = \sum_{i=1}^{m} \sum_{j=1}^{m} \frac{\partial F}{\partial \omega_i} \frac{\partial F}{\partial \omega_j} c(\omega_i, \omega_j) = \sum_{i=1}^{m} \left(\frac{\partial F}{\partial \omega_i}\right)^2 u^2(\omega_i) + 2 \sum_{i=1}^{m-1} \sum_{j=i+1}^{m} \frac{\partial F}{\partial \omega_i} \frac{\partial F}{\partial \omega_j} c(\omega_i, \omega_j) \tag{2}$$

where $c(\omega_i, \omega_j)$ is the covariance between two parameters ω_i and ω_j. The use of this method for BOS is unpractical for several reasons. Among others, we highlight the multiplicity of variables and complexity in evaluating accurately their covariances which is especially crucial and parameters-dependent in the case of cross-correlation evaluation. Furthermore, this complexity is more pronounced proportionally to the variety of mathematical procedures (Poisson, Abel inversion, ART, FBP...) that can be performed according to a specific configuration. This leads to the consequent necessity for developing their TSM formulas and quantifying the mathematical schemes induced error. This turns on a tedious task owing to the wide diversity of methods to implement each one from the aforementioned procedures such as ring method, Henkel Fourier or Fourier expansion techniques for Abel inversion implementation (Kolhe and Agrawal (2009); Pretzier (1991); Fomin (1998)). Besides, in certain applications, multiple mathematical procedures are used in combination to reconstruct the refractive index field (Hartmann and Seume (2016)). Hence, the need for a modular and

generic framework that can, in one hand, easily integrate and switch between the different reconstruction functions and, on the other hand, accounts for all possible errors regardless of their possible correlation. Therefore, in this work, we propose to implement the refraction index uncertainty analysis based on MCS.

The refractive index field uncertainty quantification methodology via MCS is depicted in Fig. 1. The proposed method involves three steps: the identification of the error sources, the generation of the input's possible values, and the evaluation of the data reduction function F.

The first step consists in identifying the error sources and specifying their respective distributions nature as well as their parameters. In BOS, similarly to PIV (Guillaume et al. (2018)), we can distinguish between two error categories which will be evaluated differently. The first category includes errors regarding the experimentally conducted measurements such as the optical layout dimensions measurement. The second category concerns the uncertainty quantification on the displacement fields in both directions, Δx and Δy, derived from cross-correlation. This part is performed through a technique adopted from the PIV community. The work-flow for this first step is detailed in Sec. 3 and Sec. 4. It should be pointed out that all errors handled along the way are considered as random errors, and that all systematic errors of known sign and magnitude have been corrected by calibration or through specific post-treatment.

During the second step, according to the nature of each error distribution, defined in the previous step, a number N_s of samples are randomly picked to generate a measurement vector for each parameter i, we name it hereafter the extended vector $\mathscr{V}_i$. So instead of being represented by a single value, each parameter will be represented by its extended vector that includes N_s samples from its corresponding distribution determined during the first step. We have chosen to create such vectors than to sample progressively, as the simulation progresses, to achieve the representativeness of the samples and to bypass the memoryless drawback in this process, and, more importantly, these vectors will be saved and will be available for use in any other uncertainty assessment as long as the same measurement tools are used. Thus, this step will only be performed once. Also, to enhance the quality of the simulation results and to decrease the computation time, we have employed the Latin Hypercube Sampling method (LHS) during this study (Stein (1987)). Furthermore, the size N_s of the extended vectors $\mathscr{V}_i$ will be overly selected, thanks to a fast implementation of LHS method, to ensure the convergence of the evaluation function F outcomes.

This evaluation is carried out in the third step through an iteration loop. Such evaluation simulates the response of the reconstruction function F under numerous inputs that considers the different error sources. During each iteration, a set of parameter values is taken from their respective extended vectors to evaluate F. All evaluation results are then saved in the refractive index extended vector $\mathscr{V}_n$ whose size increases after each iteration. This loop stops once the convergence criterion is reached; the stability of $\mathscr{V}_n$ std within 5% is considered here. Thereafter, $\mathscr{V}_n$ distribution is checked. This should be carefully considered since the distribution's type defines the way how the mean, the std values, and thus the uncertainty should be derived. Note that although the central limit theorem assumes that the distribution would be Gaussian, it doesn't guarantee its symmetry.

3 Measurement chain uncertainty

In this section, we describe the BOS experimental measurement uncertainty quantification approach.

The refraction index reconstruction through BOS requires the distance measurement from the camera to the flow and to the background, the magnification factor (M), temperature (T), pressure (p), and the medium humidity (h) (to compute the reference refractive index). During this study, we have limited our analysis to these cited errors; additional sources of error are omitted. This is due to either the difficulty of their prediction or the considerable attention or correction that was assigned to it during data processing. These include errors in the camera orientation angle relative to the background (tilt angle) or their vibrations during the experiment. To overcome this, for example, particular attention was given to their positioning and orientation, which are constantly evaluated during all stages of the experiment. On the other hand, during cross-correlation processing the displacements in both directions in areas that are not expected to have a density variation were treated as an indication of vibration (camera, background, light source). These displacements are averaged and subtracted from their respective fields. All the setup geometric distances Z_i measurements in the experiences were performed with a measuring tape with a least scale resolution equal to 1 mm. In this kind of distance reading, we estimate that the measurement can equally fall in the range of $Z_{itrue} \pm 0.5$mm, where Z_{itrue} is the unknown real distance (JCGM (2008)). Therefore, the distance measurement error follows a rectangular (uniform) distribution centered around the reported value, here the standard uncertainty u_z is Type B evaluated and is equal to $0.5/\sqrt{3}$ mm.

In this paper, we have chosen to work with a magnification factor M to illustrate the methodology, though more sophisticated calibration methods can be integrated. The magnification (M) is the conversion factor between the pixel dimensions and the physical (metric) domain. In this work, this factor was determined based on an image of a photographer ruler placed in the background plane. The factor M calculated within the camera software by dividing a known distance (read in the ruler image) by its corresponding pixels count. In this case, the various principal sources of errors that could impact the determination of this factor may be identified through its definition which can be written as:

$$M = \frac{L + e_{ruler}}{pix} \qquad (3)$$

where L is the read length on the rule, e_{ruler} is its fabrication error and pix is the number of pixels that corresponds to L. The employed ruler has a minimum scale resolution equal to 1 mm, but the reported value here is constrained by two sources of error which are the error at the origin (the so-called zero error) and the reading error. This yields to a standard uncertainty, u, equal to $2u_z$. The same reasoning leads to an estimate that the standard uncertainty on the number of pixels is constant and is equal to two pixels. For the fabrication error, e_{ruler}, we adopt the maximum permissible measurement error norm which gives an error equal to ± 0.1 mm for medium tolerance class according to DIN ISO 2768 (International Organization for Standardization (1989)). Therefore, the uncertainty associated to the ruler error is of type B and $u_{eruler} = 0.1/\sqrt{3}$ mm.

The reference refractive index n_0 is involved in the calculation of the deviation angles ε_x and ε_y in $3D$ problems and directly appears in the Poisson equation source term and Dirichlet boundary conditions (see Sec. 5.2 and 6). The computation of this value is performed via the Ciddor's equation using T, p, and h measurements. These are performed with calibrated digital sensors, in such cases, the results are subject to an error equal to ± 0.5 the last digit. This

Table 1: Experimentally conducted measurements and their respective standard uncertainties.

Source of error	Parameter	Error value	Distribution	u
Distance measurement	Z_B Z_T Z_W	± 0.5 mm	Rectangular	0.2887 mm
Magnification factor M	L	± 1 mm	Rectangular	0.5774 mm
	pix	± 2 pixel	Discrete rectangular	2 pixel
	e_{ruler}	± 0.1 mm	rectangular	0.0578 mm
Refractive index n_0	T	± 0.05 C		
	p	± 0.5 kPa	Normal	$1.00005.10^{-6}$
	h	$\pm 0.5\%$ mm		

yields an error equal to ± 0.05 C, ± 0.5 kPa and $\pm 0.5\%$ for T, p, and h measurements, respectively. Furthermore, our tests are performed under typical laboratory conditions. In such a case, the uncertainty in the refraction index n_0, inferred from both the uncertainty in the Ciddor's equation ($u_{n-ciddor}$) and from the magnitude of measurement errors (u_{n-meas}) recorded herein is about 1.10^{-8} and 1.10^{-6}, respectively (Stone and Zimmerman (2011)). Hence, u_n was calculated based on the combination of these two uncertainties (JCGM (2008)):

$$u_n = \sqrt{u_{n-ciddor}^2 + u_{n-meas}^2} \tag{4}$$

The findings of this first step are summarized in Tab. 1.

4 The displacement fields uncertainty

The displacement fields Δx and Δy are derived through a digital comparison of two images of the same pattern. One is the reference image and the other is the artificially deformed image due to the presence of the flow in-between the camera and the background. This comparison is conventionally performed by cross-correlation algorithms adopted from PIV. Although BOS images do not incorporate some of the PIV errors like out-of-plane, loss-of-pairs, or low tracer density, PIV uncertainty methods can be used in BOS experiences.

Several methods for the uncertainty quantification in PIV have been developed during recent years. Here our primary concern lies in the uncertainty associated with the processing method, namely the cross-correlation algorithm. The developed methods may be divided into a-priori and a-posteriori uncertainty quantification approaches Sciacchitano (2019). The first group, which contains the pioneering work in the field, has provided a general evaluation of the experience uncertainty by means of the measurement chain theoretical modeling which can be coupled with an evaluation of the used algorithm based on synthetic images. The second group is more specific and its scope is to quantify the uncertainty in a specific set of data. These a-posteriori uncertainty quantification approaches can also be subdivided into two subgroups: direct and indirect methods (Bhattacharya et al. (2018)).

Indirect approaches are marked by the predetermination of calibration coefficients or the creation of uncertainty surfaces from synthetic images such as the uncertainty surface method by Timmins et al. (2012) and Cross-correlation signal-to-noise ratio metrics developed by Xue et al. (2015). However, direct methods do not require predetermined information, they rely on the cross-correlation planes such as "the moment of correlation plane" (Bhattacharya et al. (2018)) or the calculated displacement fields and the original images such as the particle disparity method (Sciacchitano et al. (2013)). For more information about the different

techniques, the reader is referred to the review of the "Uncertainty quantification in particle image velocimetry" (Sciacchitano (2019)).

Given that several comparative studies have shown that the above mentioned methods perform roughly in a similar way (Bhattacharya et al. (2018); Sciacchitano et al. (2015); Boomsma et al. (2016)), we have chosen to work with "the moment of correlation plane" method proposed by Bhattacharya et al. (2018) which is the most recent published method and its integration into the open-source program PIVLab (Thielicke and Stamhuis (2014)), which is the evaluation algorithm employed during this study, is straightforward. In this approach, Bhattacharya et al.have proposed to evaluate the displacement uncertainty based on the primary peak shape in the correlation plane. Assuming that this plane is simply a convolution between the probability density function (pdf) of particle images matches and the contribution of the average particle image shape, the methodology starts by extracting this contribution from the correlation plane to obtain the pdf of possible displacement. This is expressed, in the frequency domain, by dividing the cross-correlation function by its amplitude. Then, the random and the systematic uncertainty are calculated based on the pdf spread and the peak maximum location computed thanks to curve fitting. This process is optimized by considering the shear rate and the effective number of pixels (N_{eff}) within the interrogation window (IW).

The performance of the implemented algorithm was first tested with synthetic images simulating a given situation. The simulated situations were chosen based on typical errors encountered in BOS. For each situation, images of size 1024x1024-pixels were generated and then processed with a multi-pass iterative window deformation algorithm. For each processing, 4 passes with the same IW size (128, 64, 48) were performed with an overlap factor equal to 50%. Then, on one side, all the computed displacements in a given direction (here we show the y-direction displacement $\Delta y(i, j)$) were merged into a single vector, whose size N_T is the total number of a matrix elements, from which we subtract the real displacement to obtain the total error (Eq. 5). Afterward, the Root Mean Square (RMS) of the total error was calculated (Eq. 6).

$$e_{\Delta y}(i) = \Delta_y(i) - v(i) \tag{5}$$

$$RMS(e_{\Delta y}) = \frac{1}{N_T} \sqrt{\sum_{i=1}^{N_T} e_{\Delta y}^2(i)} \tag{6}$$

where v is the true assigned displacement in y-direction. On the other side, the uncertainty on the displacements in both directions were computed and merged each into one vector and their RMS were calculated according to Eq. 7.

$$RMS(u_{\Delta y}) = \frac{1}{N_T} \sqrt{\sum_{i=1}^{N_T} u_{\Delta y}^2(i)} \tag{7}$$

Finally, the two RMS, which are intended to be equal (Sciacchitano et al. (2015)), were compared for each situation.

The findings from three different simulated situations are illustrated in Fig. 2. For the first case, the particle image size (τ) was varied in the range from 1 to 8 pixels with a step size of 0.5 pixel, a uniform displacement of 2 pixels was imposed in the y-direction ($v = 2$ pixels), and a zero-mean Gaussian white noise with std equal to 0.01 was added to the images (to simulate the camera noise). For the second case, the displacement v is shifted between 0 and 2 pixels with a step of 0.2 pixel while keeping $\tau = 3$ pixels with the same noise level as the previous case. In the last situation, the variation in noise level was simulated with a std
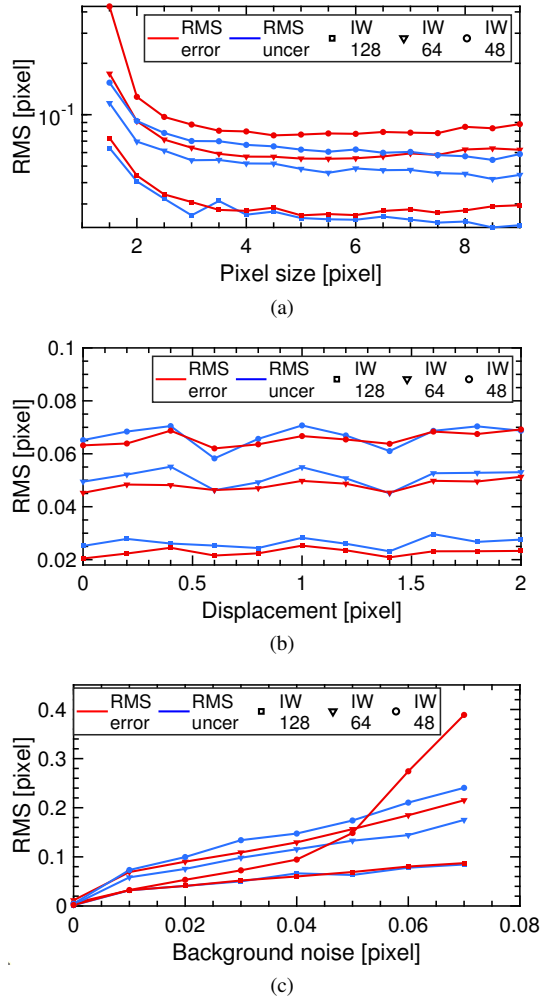
(a)

(b)

(c)

Fig. 2: RMS error and RMS uncertainty computed by the moment of correlation algorithm comparison for various simulated situations and interrogation windows.

ranging from 0 to 0.07 while keeping the particle image size constant, $\tau = 3$ pixels, and a constant and uniform displacement $v = 2$ pixels.

The examination of these graphs leads to the conclusion that the RMS uncertainties fairly match the change in the RMS error and that the quantitative comparison for all situations is largely satisfactory. Generally, the difference between the calculated error RMS and the RMS of the uncertainty derived from the moment of correlation does not exceed 0.02 pixel except in the case of IW = 48 with extreme conditions such as $\tau = 1$ pixel or a noise std $= 0.07$. This is due to the deterioration of the primary peak in the correlation plane. This method will be further evaluated in the analysis with the synthetic images in Sec. 5.
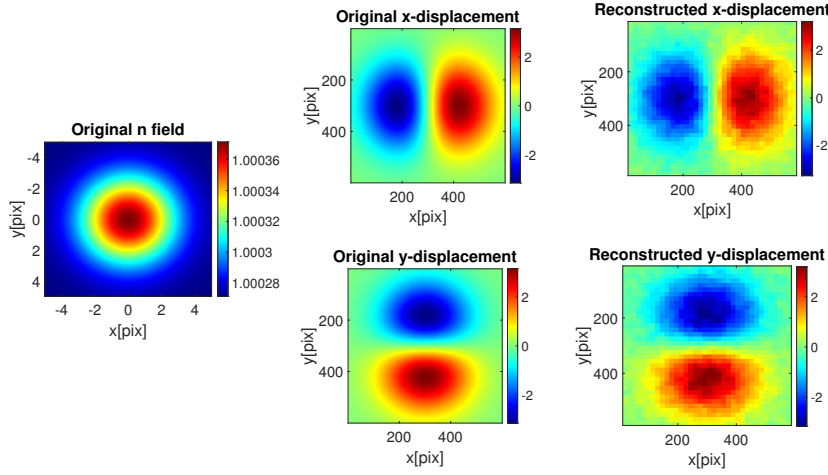
Fig. 3: Synthetic refraction index field and its induced original and reconstructed displacement.

5 Methodology assessment via synthetic images

In this section, we assess the overall BOS system uncertainty quantification methodology using synthetic images. The inspected artificial schlieren object was a flow in a cubic form with a side length equal to 10 mm. This object is composed by overlaid slices, along the z-direction, each represented by a 2d refractive index field defined by the following Gaussian distribution Fig. 3:

$$n(x,y) = n_0 + n_0.10^{-4}.exp(\frac{-x^2 - y^2}{8}) \tag{8}$$

First, based on this distribution, synthetic images (reference and distorted images) were generated. These images were produced from conclusions drawn after a PIVLab's accuracy study. Stand on this findings, we have concluded that PIVLab performs satisfactorily and compares well with results reported in bibliography. The reference image was of 600x600-pixel size with randomly distributed dots. The particle image size was chosen to be equal to 3 pixels with a density equal to 0.1 ppp. To consider the experimental noise, stemming essentially from the camera, a zero-mean-Gaussian white noise with an std = 0.01 was added to the image. The distorted image was created by shifting the reference particle image proportionally to n gradient in the x and y-direction. To simulate a typical BOS experiment layout, the flow mid-plane was considered to be placed halfway between the camera and the background, the distance separating the two latter is 1 m. The reference refraction index is set to be $n_0 = 1.000271373$ and the magnification factor is set to be M = 0.04 mm/pix with $u_M/M = 2\%$. Then, the generated images were processed with a multi-pass iterative window deformation algorithm (3 passes 64x64, 32x32, 32x32) with a constant overlap factor equal to 50%. The reference refractive index field, the real, and reconstructed displacement fields can be seen in Fig. 3.

Since the flow thickness Z_w is known, the density field 2D can be reconstructed from the projected density gradient through the density path averaging and the Poisson equation.As described in Sec. 2, the uncertainty quantification of the refractive index field reconstructed by Poisson solver was performed in three steps. First, the uncertainty on the displacement
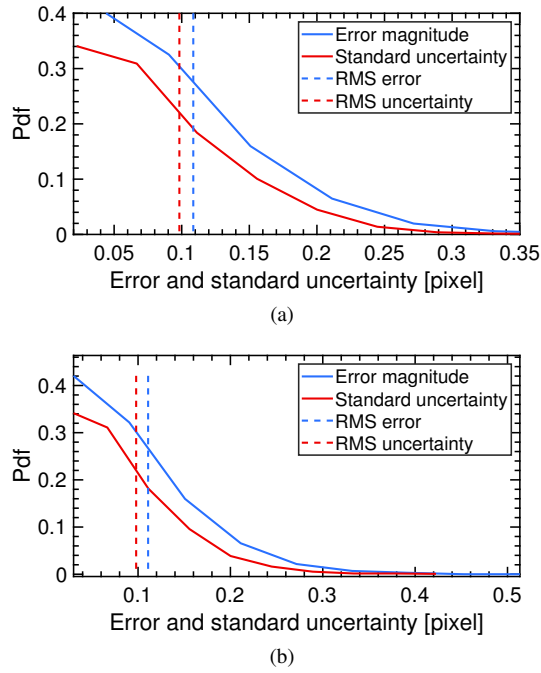
Fig. 4: Displacements errors and uncertainties probability density functions (pdf) (a) in x-direction and (b) in y-direction and their respective combined (x + y directions) error and uncertainty RMS values for the synthetic images displacements.

fields and the experimental measurements (established as a general rule in Sec. 3) was characterized. This was sampled and propagated into the source term and from the source term to the refractive index field in the second and the third step,respectively. This is further detailed in the succeeding paragraphs with a subsection discussing divergence uncertainty propagation comparison between TSM and MCS.

The displacements uncertainties were conducted by the moment of correlation algorithm (implemented and integrated onto PIVLab package). The assessment of the uncertainty quantification accuracy was once again based on the total error and the uncertainties RMS comparison. To enhance the analysis statistical representativeness, the displacements errors $e_{\Delta x}$ and $e_{\Delta y}$ were merged in a single vector (e), on one side, and the uncertainties $u_{\Delta x}$ and $u_{\Delta y}$ on a vector (u) the other side. Then, the RMS of each of these vectors, which are foreseen to be equal for an appropriate uncertainty computation, were calculated. We have obtained a very close results with RMS(e)= 0.1085 *pixels* and RMS(u) = 0.0981 *pixels*. This confirms that the displacements uncertainty quantification was conducted in a very satisfactory way. This may also be deduced from Fig. 4, where the probability density function (pdf) of the errors and uncertainties are shown with their respective RMS. From the figures, it can be noticed that the standard uncertainty distribution in both directions follows closely the correspondent displacement error, and it's clear that the errors can be covered by an expanded uncertainty.

5.1 Divergence uncertainty

This subsection aims to assess the accuracy of the developed methodology and the corresponding implemented algorithm. This was done by computing the displacement divergence and its uncertainty using the MCS and comparing the results with the analytical solution and the TSM formula, respectively. We opted to rely our assessment on the divergence computation for several reasons. First, the divergence computation involves the two displacement components and their correlations coefficients. Second, the divergence is an important element in the upcoming analysis (see Eq. 14). Third, the divergence Taylor series expansion formula is straightforward which has allowed an appropriate comparability.

The displacement components Δx and Δy in BOS experiments are measured in a 2D domain. The divergence is defined in the pixel domain as:

$$div(i,j) = \frac{\partial \Delta x(i,j)}{\partial x} + \frac{\partial \Delta y(i,j)}{\partial y} \tag{9}$$

This can be computed by applying the central difference scheme as following:

$$div(i,j) = \frac{\Delta x(i,j+s) - \Delta x(i,j-s)}{2s} + \frac{\Delta y(i+s,j) - \Delta y(i-s,j)}{2s} \tag{10}$$

with s is the grid size (in pixel).

The implemented MCS assessment was conducted as following. Firstly, The uncertainty propagation to the 2D divergence was calculated based on the uncertainty TSM propagation formula (Eq. 2) at each pixel (i,j) as a function of the displacement component uncertainty $u_{\Delta x}$ and $u_{\Delta y}$:

$$u_{div}(i,j)^2 = (\frac{1}{2s})^2 (u_{\Delta x}(i,j+s)^2 + u_{\Delta x}(i,j-s)^2 + u_{\Delta y}(i+s,j)^2 + u_{\Delta y}(i-s,j)^2$$
$$- 2c_{50} u_{\Delta x}(i,j+s) u_{\Delta x}(i,j-s) - 2c_{50} u_{\Delta y}(i+s,j) u_{\Delta y}(i-s,j)) \tag{11}$$

where c_{50} is the covariance factor between two neighboring displacements in the same direction, which was taken equal to 0.11 (Sciacchitano and Wieneke (2016)) for a cross-correlation overlap equal to 50%. In the above formulation, we considered that the error of each of the components Δx and Δy are equally spatially correlated and that the two components' errors are not correlated.

Secondly, we computed the divergence uncertainty by applying the MCS. To do so, the error of each displacement (i,j) of Δx and Δy was assumed to follow a Gaussian distribution with a mean μ corresponding to the displacement magnitude determined by the cross-correlation algorithm in that pixel and an std $\sigma(i,j) = u_{\Delta x,y(i,j)}$ determined by the moment correlation algorithm —this hypothesis is founded on central limit theorem since these errors originate from several sources—. Then, 10000 values were randomly sampled from each Gaussian distribution. Thus, we generated a 3D array in which every element (pixel) representing a displacement value ($\Delta x(i,j)$ or $\Delta y(i,j)$) was presented by its extended vector realized as previously explained. Next, the uncertainty propagation to the divergence was calculated by the evaluation of a central difference scheme at each sample. Each pixel of the divergence field will then be represented by its extended vector $\mathscr{V}_{div-MCS}$ which are the outcomes from the function evaluation at the sampled points. Finally, the mean and std deviation will be derived based on $\mathscr{V}_{div-MCS}$ distribution.

The assessment of the MCS results was carried out in three steps:

The first step consists of the simulation outputs monitoring which is essential for convergence study and $\mathscr{V}_{div-MCS}$ distribution check. The MCS convergence study based on an
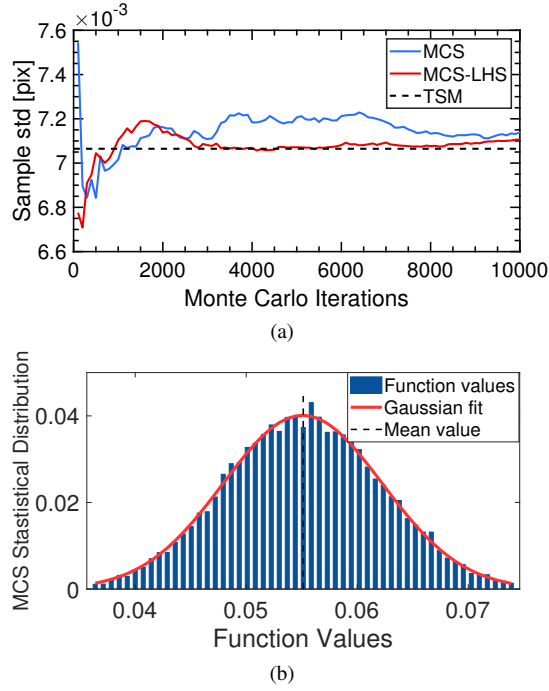
(a)

(b)

Fig. 5: MCS convergence study. (a) A sample vector std variation as a function of the simulation iteration. (b) The statistical distribution of the same vector and it's corresponding Gaussian fitting.

arbitrary vector std, for two sampling method, is shown in Fig. 5 (a), where the blue line stands for completely random sampling results, the red line represents the LHS results and the black dashed line represents the TSM value (Eq. 11) for that particular pixel. Following the two curves, we noticed that both results converged towards the same value around $7.05.10^{-3}$, here the TSM result was considered as the real value. As expected, the LHS results converge faster than the random sampling at about 3000 iterations and its relatively more accurate. Thus, indicating that the selected number of samples is largely sufficient and that LHS is a more efficient sampling method. This method will be retained for the remainder of the study. The histogram of this same vector is plotted in Fig. 5 (b) together with a Gaussian fit approximating the parent distribution. It shows that the statistical distribution of the simulation outcomes exhibits a symmetric bell-shape. Known that the outcomes follow a Gaussian distribution, which is a sample from the parent distribution, we calculated its mean ($\bar{div}_i$) and std (σ_{div})as following (Coleman and Steele (2009)):

$$\bar{div}_i = \frac{1}{N}\Sigma_{i=1}^{N}div_i \qquad (12)$$

$$\sigma_{div} = \sqrt{\frac{1}{N-1}\Sigma_{i=1}^{N}(\bar{div}_i - div_i)^2} \qquad (13)$$

where N is the number of the evaluations (the needed number to reach the convergence) and div_i is the individual outcome from the ith iteration. Referring to the uncertainty definition,
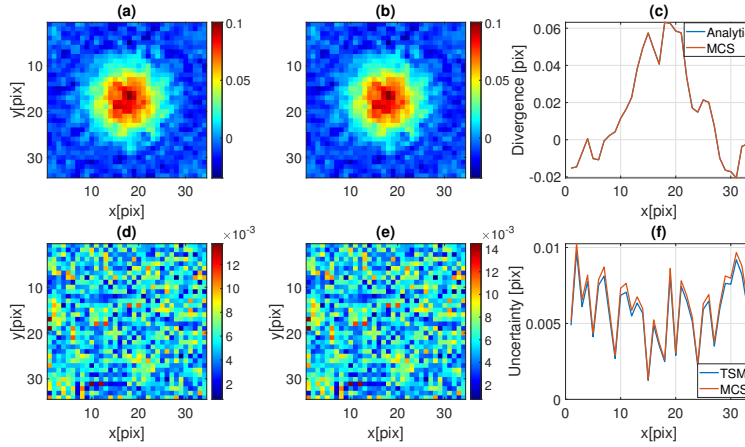
Fig. 6: Displacement divergence and its associated uncertainty. (a): the divergence calculated by central difference scheme, (b): by MCS, (c): cross-sectional comparison in the middle of the filed, (d): TSM uncertainty, (e): MCS uncertainty, (f): cross-sectional comparison in the middle of the field.

the divergence uncertainty $u_{div} = \sigma_{div}$.

The second step in MCS assessment consists of the comparison between the analytically calculated divergence and that which was determined by MCS method. Both fields should show identical values (at least very close). Fig. 6 (a) displays the divergence field calculated as a function of the displacement fields Δx and Δy by direct application of the central difference scheme. Fig. 6 (b) displays the one calculated by MCS (the mean of each vector $\mathscr{V}_{div-MCS}$) alongside with a cross-sectional comparison of the divergence in the middle of the field where the highest gradient occurs. The examination of these profiles reveals a complete match between the two results. This confirms the accuracy of the MCS method and the above-mentioned convergence and distribution study as well as the application of the Eq. 12 for mean calculation.

The last step of our assessment consists in comparing the results of the uncertainty propagation computed with the two methods. The bottom part of the same figure shows a comparison between the divergence standard uncertainty computed by TSM and MCS and a cross-sectional comparison in the center of the field. Here, the correspondence is excellent with quite minimal discrepancy which is likely due to the truncation error of TSM and the approximations made on the choice of the cross-correlation coefficients. This rather satisfactory observation is an indication of the appropriateness of the adopted assumptions, the sampling method, and the use of the Eq. 13 for the std calculation.

5.2 Uncertainty propagation in 2D refraction index field using Poisson equation

In BOS experiment, the investigated flow's refraction index distribution is proportional to the measured displacements and it can be reconstructed by solving the following Poisson
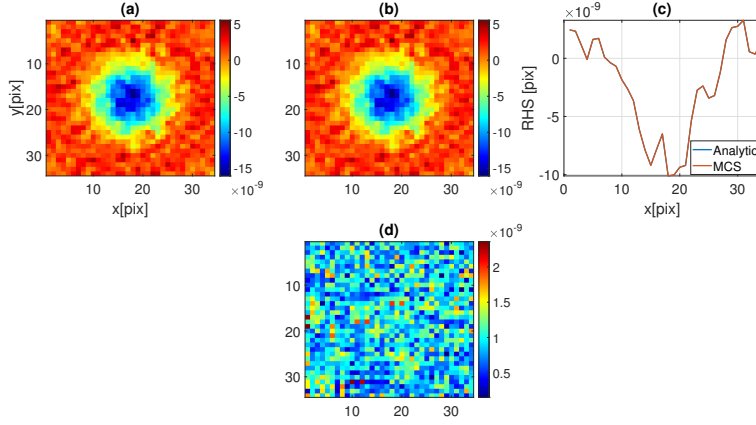
Fig. 7: Poisson equation source term and its associated uncertainty. (a): the analytic solution, (b): MCS result, (c): cross-sectional comparison in the middle of the filed, (d): the source term uncertainty.

equation in the pixel domain (Vinnichenko et al. (2012)):

$$\begin{bmatrix} \frac{\partial^2 n}{\partial^2 x} \\ \frac{\partial^2 n}{\partial^2 y} \end{bmatrix} = \frac{2MM_{obj}n_0}{Z_w(Z_w + 2Z_B)} \begin{bmatrix} \frac{\partial \Delta x}{\partial x} \\ \frac{\partial \Delta y}{\partial y} \end{bmatrix} \tag{14}$$

where M_{obj} denotes the magnification factor in the object plan and it can be expressed as:

$$M_{obj} = M \frac{(Z_T - (Z_B + (Z_W/2)))}{Z_T} \tag{15}$$

where Z_B and Z_T denotes, respectively, the distances that separate the flow middle plan, whose width Z_W, from the background and the camera. The divergence extended array in the right-hand side term was calculated flowing the process underlined in Sec 5.1. Similarly, for all other parameters, the respective extended vector was generated through LHS from their respective error distribution centered around the measured value. To compute the source term S, these vectors together with the divergence extended matrix were then applied to evaluate a function that has the same form of the right-hand side in Eq 14. After ascertaining the convergence of the simulation and the symmetrical Gaussian distribution of its outcomes, we compared the directly calculated source term (the analytic solution using the measured values and the displacement fields) against the mean Eq 12 of the MCS's result. The results together with the source term standard uncertainty (u_s) are shown in Fig. 7. It can be seen that, as expected, the two fields match perfectly. The S extended matrix, which is the outcome of this simulation, was used as input of the final simulation (Poisson solver evaluation).

Obviously, the solution of Eq 14 requires adequate boundary conditions (Dirichlet/Neumann) specification. For the sake of generality, in this example, we used mixed boundary conditions. The Neumann boundary condition is given by:

$$\frac{\partial n}{\partial \chi_\perp} = \frac{2MM_{obj}n_0 \Delta \chi_\perp}{Z_w(Z_w + 2Z_B)} \tag{16}$$

where $\Delta\chi_\perp$ is the displacement component normal to the boundary. The top and bottom Neuman boundaries extended vectors were derived as previously mentioned with respect to the displacement normal to those boundaries, the experimentally conducted measurements and their respective associated errors. The Dirichlet boundaries extended vector were obtained by evaluating the exact equation (Eq. 8) as a function of the n_0 extended vector. The MCS, which consists of the evaluation of second-order central differentiation scheme function, was conducted using the built source term and its mixed boundary conditions. The simulation results were tracked, and we concluded that the outcomes converge at around 4000 iterations and it follows a normal symmetric distribution. Hence, we calculated the mean and the std following Eq. 12 and Eq. 13. Furthermore, for such sample distribution, the uncertainty on the mean follow a t-distribution whose parameters approach the Gaussian ones regarding the sufficiently large number of samples employed herein (Coleman and Steele (2009)). Thus, the expanded uncertainty $U_{n95\%}$ corresponding to a 95% confidence interval was obtained by a coverage factor $k_{95\%} = 1.96$.

To assess the potential of the proposed framework, a comparison between the reconstructed and the true cross-sectional refraction index profiles is shown in Fig. 8, together with the expanded uncertainty $U_{n95\%}$. It can be inferred that the reconstructed and the real profiles are fairly close and, more importantly, the real value is all over covered by the expanded uncertainty. This findings indicates the appropriateness of the hole process ranging from the sampling passing by the central differentiation scheme, the boundary conditions and the mean calculation. These profiles can be divided into two parts; the first part covers the left and right boundaries, here the 4 curves merge into one which is due to the application of the Dirichlet boundary conditions at these borders, thereby raising the results accuracy locally. Therefore, we may conclude that the estimated error on the refractive index does not have a significant effect on the final solution as it is much lower compared to any other errors. The second group covers the summit area, here the solution is governed by the Neumann boundary conditions and the refractive index gradient is higher in the center of the volume. In this area, the offset between the reconstructed and the real profile is more pronounced but remains consistently covered by the 95% confidence bounds corridor. It is worth mentioning that the uncertainty propagation quantification in this case, besides to directly considering the measurement errors, it implicitly accounts for additional features. This concerns the truncation error of the employed mathematical scheme and the possible correlated variations among the measured variables. Note that the latter property is a major strength of this method because it spares the difficult challenge in identifying all possible correlations and in their covariance coefficients quantification. In more general terms, the uncertainty calculation by evaluating the distribution of the data reduction equation response for multiple measures, the statistical method, is qualified as more accurate than TSM equation when a correlation is present (JCGM (2008)).

6 Uncertainty propagation in $3D$ axisymmetric refraction index field with experimental images

We now turn to an illustration of both the modularity and the feasibility of the proposed methodology in the case of $3D$ axisymmetric flow.

For this purpose, we conducted a BOS experiment to quantitatively visualize the flow field around a transonic projectile in free-flight. The projectile was a .338-inch caliber (diameter) freely flying at Mach $Ma = 1.2$. A background was developed with optimum characteris-
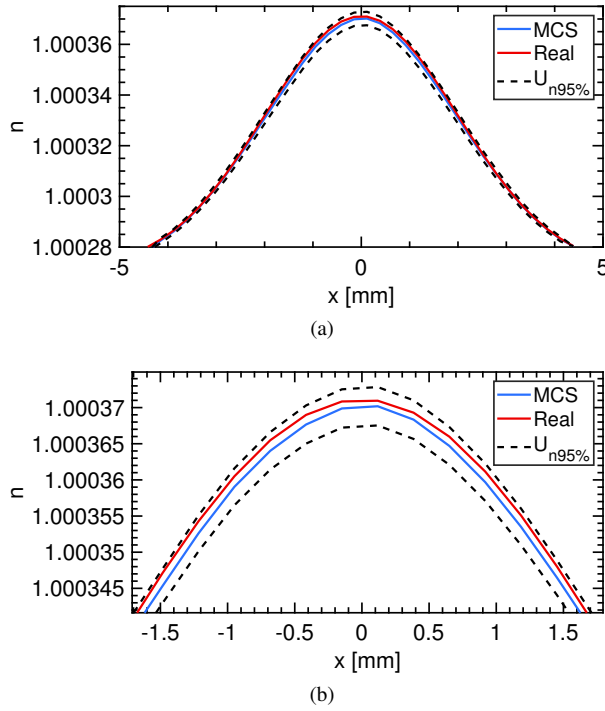
(a)

(b)

Fig. 8: Comparison between Monte Carlo method (MCM) results and the real solution together with the expanded uncertainty interval ($U_{n95\%}$). (a): cross sectional comparison in the middle of the field of view. (b): close up of the central area.

tics and printed on a transparency. Then, it was taped on a Plexiglas mounted on a relatively heavy metal frame to reduce the vibration. The assembly was positioned at a distance Z_B (see Tab. 2) from the assumed projectile trajectory. The projectile velocity was measured using a velocity light gate. A high-speed camera type Photron FASTCAM SA5 was used during the experiment. Two images were selected after each firing. To minimize the effect of vibration caused by the shooting, we considered the last image taken just before the projectile's first appearance in the camera's field of view as the reference image. The experimental setup and the employed projectile schematics are shown in Fig. 9.

We processed the image pair using PIVLab with a multi-pass iterative window deformation algorithm (3 passes 64x64, 32x32, 16x16) with an overlap factor equal to 50% without smoothing nor outliner detection. Then we averaged the displacements on the supposedly undisturbed area, and we subtracted it from their respective displacement fields. As well, we calculated the uncertainties on the displacements thanks to the moment of correlation algorithm previously described.

In BOS experiments, assuming that the projectile's flow field is axisymmetric, with the x-axis as the axis of symmetry, and the z-axis as the optical axis. Here the symmetry axis is seen as known with certitude, i.e. the axis of symmetry of the projectile, in different situations the selection of this axis position may be considered as an error source and may be integrated in the framework. Thanks to its axisymmetry, it can be observed that the di-
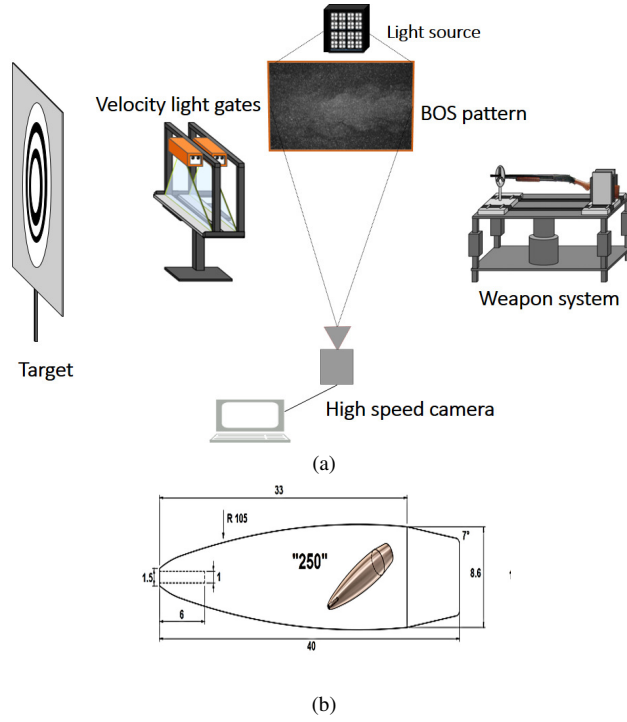
(a)

(b)

Fig. 9: BOS experimental setup (a) for the flow field visualization around a (b) .338-inch caliber projectile: HPBT (Hollow Point Boat Tail) 250 grains model bullets.

Table 2: Experimental setup parameters

Component	Parameter	Value
Experimental setup	Z_B	977 mm
	Z_T	2855 mm
	L	300 mm
	pix	710 pixel
	n_0	1.000271373
Camera	Focal length f	135 mm
	Aperture (f -number)	8
	Shutter Speed	1/91000 s
	Frame rate	15000 fps
	Image Width x Height	768 x 648 pixel

mensions of the problem now depend only on $r = \sqrt{y^2 + z^2}$ and x. The components of the measured deflection angle, ε_x and ε_y, can be formulated into cylindrical coordinates such as (Fomin (1998)):

$$\varepsilon_x(x,y) = \frac{2}{n_0} \int_{r=y}^{R} \frac{\partial n}{\partial x} \frac{r dr}{\sqrt{r^2 - y^2}} \tag{17}$$

$$\varepsilon_y(x,y) = \frac{2y}{n_0} \int_{r=y}^{R} \frac{\partial n}{\partial r} \frac{dr}{\sqrt{r^2 - y^2}} \tag{18}$$

The integrals of equations Eq. 17 and Eq. 18 are both of Abel form, but of a different nature. Their inverses have been also computed differently for each abscissa x and each radial position r, from the symmetry axis previously defined to the edge of the acquisition field, to obtain $\frac{\partial n}{\partial x}$ and $\frac{\partial n}{\partial r}$, respectively. Based on the geometry in Fig. 1 and assuming a paraxial recording and small angular ray deflection angle ε_y can be written as (Raffel (2015)):

$$\varepsilon_x = \frac{\Delta x'}{Z_B} = M \frac{\Delta x}{Z_B} \tag{19}$$

$$\varepsilon_y = \frac{\Delta y'}{Z_B} = M \frac{\Delta y}{Z_B} \tag{20}$$

with $\Delta x'$ and $\Delta y'$ are the displacements in the x- and y-directions in the background plane. Then the refractive index field n can be calculated by solving the Poisson equation in cylindrical coordinates. However, due to the presence of the projectile in the integration domain and that it is mathematically inconceivable to crop it in the symmetry axis, we employed an inverse gradient method based on least squares optimization which is mathematically equivalent to solving the Poisson equation.

The uncertainties on experimental measurements were reproduced as indicated in their dedicated section except for the uncertainty on Z_B. The particularity here is that the trajectory of the projectile cannot be determined with precision, in this type of projectile (specific for sniper) and for the distance that separating the camera-background from the weapon, the uncertainty on the projectile position is estimated of $u_{projectile} = 0.5$ mm which results in u_{Z_B} being calculated based on the combination of these two uncertainties with a Gaussian error distribution (JCGM (2008)):

$$u_{Z_B} = \sqrt{u_{projectile}^2 + u_Z^2} \tag{21}$$

Here, similarly to the synthetic image's treatment, the extended vectors of each parameter were created based on their respective distributions. Then, these vectors were used to evaluate two functions corresponding to Eq. 19 and Eq. 20 to compute the extended matrices of ε_x and ε_y. These matrices will serve as inputs for the two Abel inversion algorithms. These were implemented according to the ring method where the unknown gradient of the refractive index field is subdivided in N rings with the assumption that within one annular zone the refraction index is constant (Fomin (1998)). The outputs of this step, the extended matrices of $\frac{\partial n}{\partial x}$ and $\frac{\partial n}{\partial r}$, together with $\mathscr{V}_{n_0}$ were used as the two surface gradients and the constant of integration, respectively. The simulation convergence was achieved after approximately 2000 iterations and all outcome vectors follow Gaussian distributions whose mean and std were calculated according to the Eq. 12 and Eq. 13.

Furthermore, MCS results were used to assess the accuracy of a numerical simulation. A Computational Fluid Dynamics (CFD) analysis was done using steady RANS simulation with a low-order turbulence model including transition with ANSYS Fluent 19.R1. Those results were intended to do a first iteration comparison with the BOS technique, in order to bring to light the possibility to quantify the density jumps of very precise phenomena. Detailed investigations were conducted to assess modeling sensitivities (including a grid sensitivity study) and limitations at transonic velocity regarding the numerical and aerodynamic parameters. The final mesh used to visualize the development of the shock waves for the steady RANS simulations of the full projectile in free-air consists typically of 7 million elements with a prismatic boundary layer mesh comprising 20 layers resulting in an average value for y^+ of 1 along the adiabatic no-slip walls. The domain extends to 20 projectile-lengths where pressure-far-field conditions were applied.
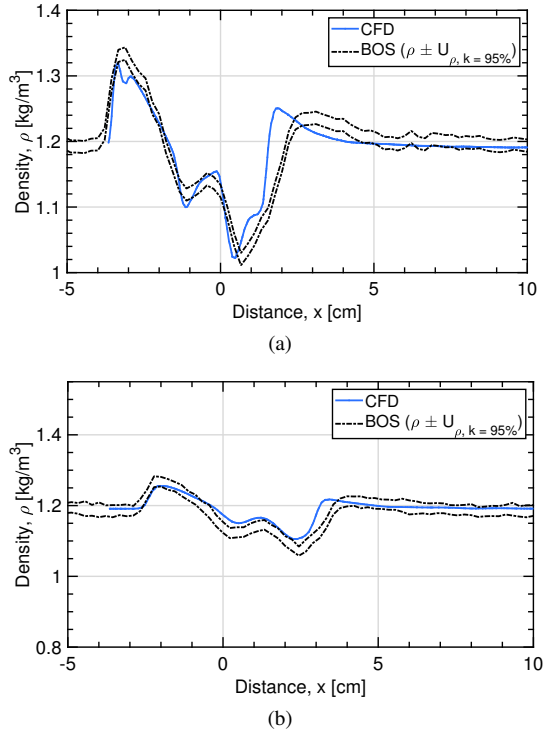
(a)

(b)

Fig. 10: Comparison of cross-sectional expanded uncertainty density profile obtained through BOS (experiment) and CFD for a transonic projectile $Ma = 1,2$ at two level; (a): $y = 10$ mm, (b): $y = 30$ mm, the x-axis being oriented along the axis of symmetry of the projectile with the origin located at the center of its base

In BOS, the density was calculated thanks to Gladstone-Dale equation offering a relationship between the refraction index and the density (Fomin (1998)):

$$n - 1 = G(\lambda)\rho \tag{22}$$

where ρ is the density and G is the Gladstone-Dale constant, weakly dependent on the light wavelength λ, which is taken as constant at 550 nm. This value was assumed to be known with much smaller error than the conducted measurement and its uncertainty is negligible. The density expanded uncertainty $u_{\rho 95\%}$ corresponding to a 95% confidence interval was obtained by a coverage factor $k_{95\%} = 1.96$.

The comparison between the cross-sectional profiles of the density expanded uncertainty at different radial distances and the CFD results are shown in Fig. 10. We noticed a mostly acceptable matching between the different profiles; we observed in both cases the specific N-shape pattern due to compression-expansion at the shock and expansion waves before returning to the ambient density. Both techniques have successfully detected the different chocs with very close magnitude and positions. Besides, for the most part, the CFD profile is within the confidence interval, except for few offsets. A closer inspection of these profiles reveals that differences are mostly in the vicinity of steep gradients, related to the presence

of the shock waves, which is probably due to a spatial filtering effect related to the cross-correlation (Raffel et al. (2018)). This is a fairly known phenomenon associated with these algorithms and is probably not well accounted for in the displacement uncertainty quantification method. A part of the difference is, undoubtedly, due to numerical modeling errors that are under investigation for future studies.

7 Conclusion

In this work, we have presented a modular framework for a-posteriori uncertainty quantification of the refraction index and density field in BOS based on MCS. That is, to the authors' best knowledge, the first work that considers all error sources instead of only focusing on the displacement field errors. The model has been implemented through three steps.

First, the determination of the experimental and displacement related errors and their respective distributions. During this study, We have presented a comprehensive analysis of the experimental measurement chain. Indeed, we have pinpointed the main experimental error sources, and we have identified and quantified their uncertainties. To compute displacement uncertainty we have taken benefit from the new displacement uncertainty method named the moment of correlation plane .

Second, the sampling of error distributions using the LHS method to create extended vectors. This method has proven to be more efficient than random sampling regarding accuracy and computation time.

Finally, the errors were propagated to the solution using MCM. This was realized by simulating a given reconstruction function response while submitted to the extended vector inputs. The response behavior has been tracked to evaluate its convergence and its distribution. Then, according to this distribution type, the uncertainty propagation has been quantified.

We have demonstrated and tested these different steps with the help of a synthetic refractive index field based on which we have simulated a typical BOS experiment. The refractive index field was reconstructed using a Poisson solver under mixed boundary conditions. From the results, the accuracy and simplicity of the technique have been demonstrated. Furthermore, this method has been seen to be extremely flexible owing to the ease of integration of a different construction procedure, which is the Abel inversion. We have demonstrated this aspect using a BOS experimental setup for visualizing the flow around a .338 caliber projectile in transonic free-flight. Both BOS and CFD results successfully captured the specific N-shape for the shock expansion pattern. The density profiles were very close except for small deviations that can be attributed to drawbacks in numerical simulation and cross-correlation algorithms. Given that Abel inversion is a specific application of the FBP and ART, the same approach can be extended for the applications of those procedures.

Moreover, the exemption from the mandatory requirement of error correlation coefficients determination, whose existence is evident and parameters-dependent in the cross-correlation processing, is one of the strong points of this implementation. Additionally, evaluating the function itself repeatedly to determine its uncertainty takes into account the employed mathematical procedure error which is not directly addressed elsewhere.

The necessary time to perform the simulations constitutes the weak aspect of the method. In general, the simulation time depends on the numerical scheme to be evaluated and remains comparable with the uncertainty evaluation techniques on displacements. Actually, such constraints are no longer a real problem nowadays given CPU and memory improvements, this is mostly viewed as an impediment exclusively in real-time applications.

References

Azijli I, Sciacchitano A, Ragni D, Palha A, Dwight RP (2016) A posteriori uncertainty quantification of PIV-based pressure data. Exp Fluids 57(5):72, DOI 10.1007/s00348-016-2159-z

Bhattacharya S, Charonko JJ, Vlachos PP (2018) Particle image velocimetry (PIV) uncertainty quantification using moment of correlation (MC) plane. Meas Sci Technol 29(11):115301, DOI 10.1088/1361-6501/aadfb4

Boomsma A, Bhattacharya S, Troolin D, Pothos S, Vlachos P (2016) A comparative experimental evaluation of uncertainty estimation methods for two-component PIV. Meas Sci Technol 27(9):094006, DOI 10.1088/0957-0233/27/9/094006

Coleman HW, Steele WG (2009) Experimentation, Validation, and Uncertainty Analysis for Engineers, 3rd edn. John Wiley & Sons, Hoboken, N.J, oCLC: 310400087

Fomin NA (1998) Speckle Photography for Fluid Mechanics Measurements. Experimental Fluid Mechanics, Springer, Berlin, oCLC: 845092443

Guillaume G, Beaulieu C, Braud P, David L (2018) Démarche d'estimation des incertitudes en PIV basée sur la méthode GUM. In: CFTL-16, CNRS,IRSN, Sep 2018, Dourdan, France, p 10

Hargather MJ, Settles GS (2010) Natural-background-oriented schlieren imaging. Exp Fluids 48(1):59–68, DOI 10.1007/s00348-009-0709-3

Hartmann U, Seume JR (2016) Combining ART and FBP for improved fidelity of tomographic BOS. Meas Sci Technol 27(9):097001, DOI 10.1088/0957-0233/27/9/097001

International Organization for Standardization (1989) ISO 2768-1, General tolerances Part 1: Tolerances for linear and angular dimensions without individual tolerance indications. Tech. rep., ISO

JCGM (2008) BIPM - Guide to the Expression of Uncertainty in Measurement (GUM). Tech. rep., JCGM

JCGM J (2008) 101: 2008 evaluation of measurement data–supplement 1 to the "guide to the expression of uncertainty in measurement"–propagation of distributions using a monte carlo method. International Organisation for Standardisation, Geneva

Kolhe PS, Agrawal AK (2009) Abel inversion of deflectometric data: Comparison of accuracy and noise propagation of existing techniques. Appl Opt 48(20):3894, DOI 10.1364/AO.48.003894

Meier GEA (1998) New optical tools for fluid mechanics. Sadhana 23(5-6):557–567, DOI 10.1007/BF02744579

Moumen A, Grossen J, Ndindabahizi I, Gallant J, Hendrick P (2020) Visualization and analysis of muzzle flow fields using the Background-Oriented Schlieren technique. J Vis pp 1–15, DOI 10.1007/s12650-020-00639-w

Pan Z, Whitehead J, Thomson S, Truscott T (2016) Error propagation dynamics of PIV-based pressure field calculations: How well does the pressure Poisson solver perform inherently? Meas Sci Technol 27(8):084012, DOI 10.1088/0957-0233/27/8/084012

Pretzier G (1991) A New Method for Numerical Abel-Inversion. Zeitschrift für Naturforschung A 46(7):639–641, DOI 10.1515/zna-1991-0715

Raffel M (2015) Background-oriented schlieren (BOS) techniques. Exp Fluids 56(3):60, DOI 10.1007/s00348-015-1927-5

Raffel M, Willert CE, Scarano F, Kähler CJ, Wereley ST, Kompenhans J (2018) Particle Image Velocimetry: A Practical Guide, third edition edn. Springer, Cham

Rajendran LK, Zhang J, Bhattacharya S, Bane SPM, Vlachos PP (2019) Uncertainty Quantification in density estimation from Background Oriented Schlieren (BOS) measurements. Meas Sci Technol (1):25, DOI 10.1088/1361-6501/ab60c8

Sciacchitano A (2019) Uncertainty quantification in particle image velocimetry. Meas Sci Technol 30(9):092001, DOI 10.1088/1361-6501/ab1db8

Sciacchitano A, Wieneke B (2016) PIV uncertainty propagation. Meas Sci Technol 27(8):084006, DOI 10.1088/0957-0233/27/8/084006

Sciacchitano A, Wieneke B, Scarano F (2013) PIV uncertainty quantification by image matching. Meas Sci Technol 24(4):045302, DOI 10.1088/0957-0233/24/4/045302

Sciacchitano A, Neal DR, Smith BL, Warner SO, Vlachos PP, Wieneke B, Scarano F (2015) Collaborative framework for PIV uncertainty quantification: Comparative assessment of methods. Meas Sci Technol 26(7):074004, DOI 10.1088/0957-0233/26/7/074004

Stein M (1987) Large Sample Properties of Simulations Using Latin Hypercube Sampling. Technometrics 29(2):143–151, DOI 10.2307/1269769

Stone JA, Zimmerman JH (2011) Engineering metrology toolbox. URL http://emtoolbox nist gov/Wavelength/Edlen asp 20:24

Thielicke W, Stamhuis E (2014) PIVlab – Towards User-friendly, Affordable and Accurate Digital Particle Image Velocimetry in MATLAB. J Open Res Softw 2(1):e30 DOI http://dx.doi.org/10.5334/jors.bl

Timmins BH, Wilson BW, Smith BL, Vlachos PP (2012) A method for automatic estimation of instantaneous local uncertainty in particle image velocimetry measurements. Exp Fluids 53(4):1133–1147, DOI 10.1007/s00348-012-1341-1

Vinnichenko NA, Uvarov AV, Plaksina YY (2012) Accuracy of background oriented schlieren for different background patterns and means of refraction index reconstruction. In: ISFV-15, Minsk, Belarus, p 15

Xue Z, Charonko JJ, Vlachos PP (2015) Particle image pattern *mutual information* and uncertainty estimation for particle image velocimetry. Meas Sci Technol 26(7):074001, DOI 10.1088/0957-0233/26/7/074001